

Identification of the steady-state creep behavior of Zircaloy-4 claddings under simulated Loss-Of-Coolant Accident conditions based on a coupled experimental/numerical approach

D. Campello^a, N. Tardif^a, M. Moula^a, M.C. Baietto^a, M. Coret^b, J. Desquines^c

^a*Université de Lyon, CNRS, INSA-LYON, LaMCoS UMR 5259, 20 Avenue Albert Einstein, F69621 Villeurbanne Cedex, France*

^b*GeM (UMR 6183), École Centrale de Nantes, 1 rue de la Noë 44321 Nantes, France*

^c*IRSN/PSN-REX/SEREX/LE2M, Saint Paul lez Durance, France*

Abstract

The secondary creep behavior of Zircaloy-4 (Zr-4) claddings under simulated Loss-Of-Coolant Accident (LOCA) conditions is investigated. A coupled experimental / numerical approach is developed in order to determine the steady-state creep constitutive law's parameters. The test matrix targets thermal mechanical conditions for which several creep mechanisms are expected to take place (phase transition zone of Zr-4).

Ballooning tests were performed on tubular specimens. A heterogeneous thermal mechanical loading was applied to the specimen. The resulting thermal and kinematics fields were measured by full field optical measurements. Then a Finite Element model was updated in order to determine a constitutive Norton creep law fitting the kinematic fields measured by a digital image correlation (DIC). The following methodology enables a significant reduction in the number of tests used for the mapping of creep mechanisms depending

on stress and temperature conditions. The results of nine experiments covering stresses from 7 to 45 MPa and temperatures varying from 745 to 850 °C are detailed. In the α -phase domain, the transition from low Norton exponents (~ 1) to higher ones (~ 4 -5) is observed at a von Mises stress of 26 MPa. The activation energies are consistent in the α -phase domain. For modeling purposes, several tests ($T < 810$ °C) are then correlated. Three constitutive laws, depending on the stress and creep-rate levels, were determined. Norton exponent and activation energy consistent with the superplasticity observed by Garde *et al.* were identified in the early stage of the two-phase domain.

Keywords: Zircaloy-4, LOCA, Ballooning tests, FEMU

1. Introduction

After Fukushima accident in March 2011, increasing attention has been given to nuclear reactor core coolability. The full analysis of a LOCA requires complex coupled physical modeling including thermal-hydraulics and mechanical behaviors of fuel rods. During its operating life, the water in the primary loop of a Pressurized Water Reactor (PWR) is pressurized at 155 bar and heated by fuel pellet stacks up to 320 °C. The fuel claddings are also internally pressurized by fission gas and fission gas release. When a breach appears in the loop, the water is depressurized limiting the coolant efficiency. Both the water and the fuel rods are then heated and the claddings are loaded with internal pressure. It can lead to rod ballooning and, potentially, to rod bursting. Re-flooding the nuclear core reactor interrupts this accidental sequence. The fuel rod ballooning can impede the core cooling capacity by flow blockage.

Until the cladding bursts and reaches the nearby fuel rods, a relatively constant plane stress loading is representative of hypothetical LOCA conditions. In the present study, secondary creep data are quantified from Zircaloy-4 (Zr-4) cladding internally pressurized at high temperature (up to 850 °C).

The PERFROI program [1] aims at improving the thermal-hydraulic-mechanical modeling of the entire nuclear reactor core during a postulated LOCA. Several aspects involved in the burst of the LOCA are independently studied in order to further understand the interactions between several fuel rods. The present study focuses on the secondary creep behavior of Stress Relieved Annealed (SRA) Zr-4.

Cladding temperature during a LOCA can reach up to 1200 °C. The steady-state creep behavior of Zr-4 claddings is here investigated for temperatures around the phase transformation from α to $(\alpha + \beta)$ -phase (ranging from 750 to 850 °C) [2]. Cladding micro structure is modified by irradiation under normal operations, however, irradiation damages are annealed early in the ballooning phase of a LOCA [3]. The specific influence of some other parameters such as corrosion and hydriding will not be discussed in this paper.

The secondary creep behavior of as-received Zr-4 is usually [4, 5] modeled using a power-law detailed in equation (1). The temperature T and stress σ influence on the steady-state creep-rates $\dot{\epsilon}_{ss}^p$ are respectively defined by the activation energy Q and the Norton exponent n :

$$\dot{\epsilon}_{ss}^p(\sigma, T) = A \cdot \sigma^n \cdot \exp\left(-\frac{Q}{R.T}\right), \quad (1)$$

with A being a third material parameter. Creep mechanisms directly influence n and Q creep parameters. In the α -phase domain, Norton exponents close to 1 are associated with a diffusion creep mechanism whereas for $n \in [4 - 6]$ a dislocation mechanism prevails [6, 7, 4]. Concerning the activation energy Q , possible creep mechanisms diffusion and dislocation are identified for values ranging respectively from 50 to 150 kJ/mol and 20 to 300 kJ/mol. Few data address the creep behavior in the $(\alpha + \beta)$ -phase domain, beginning at 810 °C for as-received Zr-4.

The experimental setup described in Campello *et al.* [8, 9, 10, 11] allows to perform uniaxial tests on Zr-4 alloys at a hoop stress ranging from 5 to 55 MPa, for temperature ranging from 750 to 850 °C. The results provided steady-state creep rate and temperature axial distribution along with the specimen. The rich database was then fully analyzed using Finite Element Model Updating (FEMU) in order to identify the creep parameters. Material behavior identification is increasingly assisted with FEM [12, 13] for solving inverse problem. FEMU, originally performed by Kavanagh and Clough in [14], relies on an error minimization approach in order to match as fairly as possible observed and the calculated data. The cost function choice is particular to the experimental setup and processing data method [15, 16] as much as the constitutive behavior law to be identified.

By coupling high resolution kinematics and thermal fields addressing to heterogeneous thermal-mechanical conditions, the methodology proposed is able to accurately determine secondary creep parameters in a local stress and

temperature domain. It also significantly reduces the number of tests needed to map the constitutive parameters according to the thermal-mechanical conditions of interest, and the associated random errors.

This paper first details for each test the experimental setup and the data processing providing creep-rate and temperature profiles along the Region Of Interest (ROI) [8]. The test’s modeling and the identification algorithm are then detailed, and validated. An experiment performed at 850 °C is itemized, and the modeling options are discussed. Finally, the results of nine experiments are detailed and the influence of temperature and stress are demonstrated in the tested thermal-mechanical conditions. Data from several experiments are correlated in order to identify the parameters of three constitutive creep-laws addressing possible diffusion and dislocation creep mechanisms governing the deformation in the α -phase domain.

2. Material and methods

The specimens were 90 mm long SRA Zr-4 (see the chemical composition in Table 1) claddings tube samples cut by an electro discharge machining.

Table 1: Stress Relieved Annealed Zircaloy-4 nominal chemical composition (in wt.%)

Sn	Fe	Cr	O	C	Zr
1.29	0.21	0.11	0.13	0.016	bal.

The cladding outer radius is 4.75 mm, and wall thickness w is 0.57 mm. Eccentricities Ξ were evaluated between 1 and 3% using equation (2). This rather small eccentricity prevents the specimen from early non-axisymmetric

localization during the test.

$$\Xi = \frac{w_{max} - w_{min}}{w_{max} + w_{min}} \quad (2)$$

Link *et al.* also reported such measurements in [17].

2.1. Test procedure and setup

The test sample was connected onto a 10 kN servo-hydraulic tensile machine using custom grips [18]. An enclosure was fitted to the machine to perform the tests under inert environment (see Figure 1).

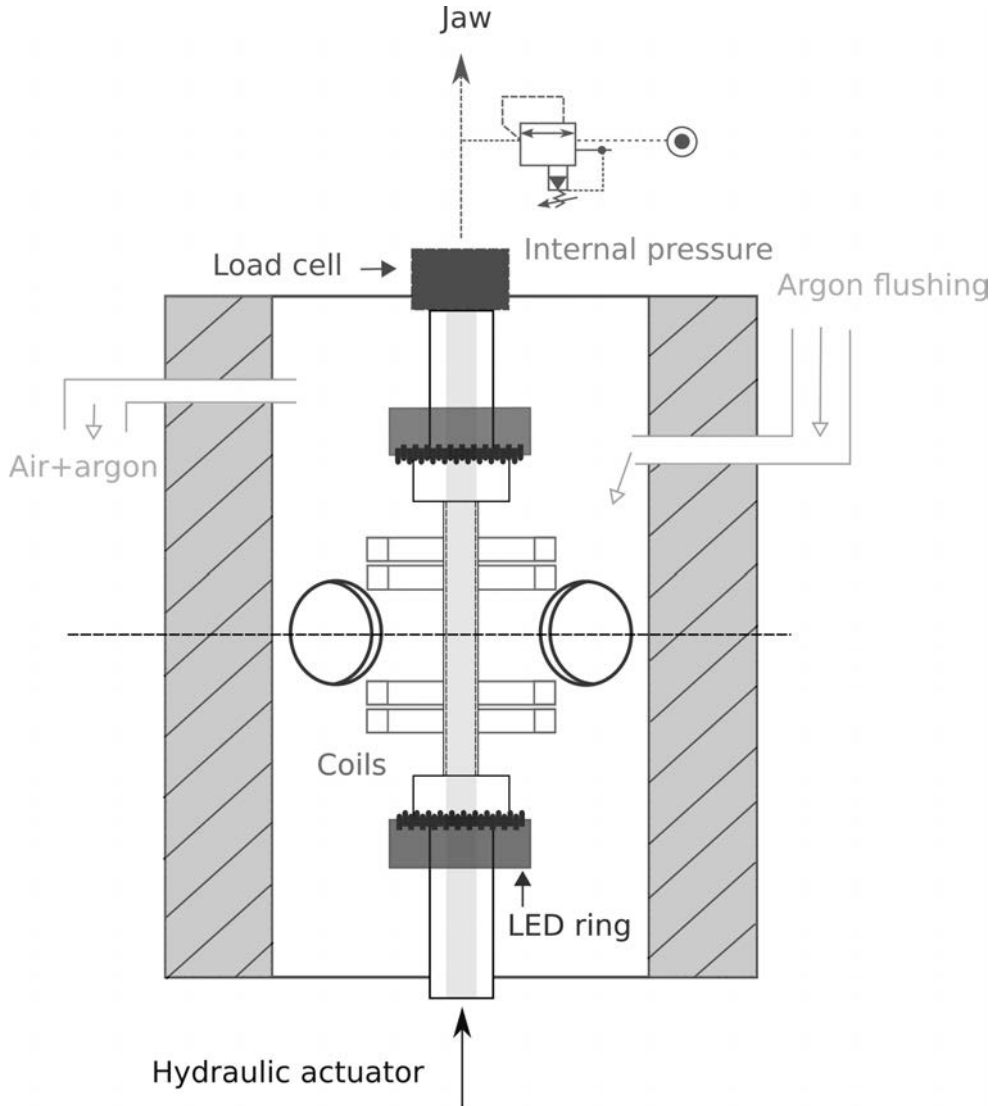
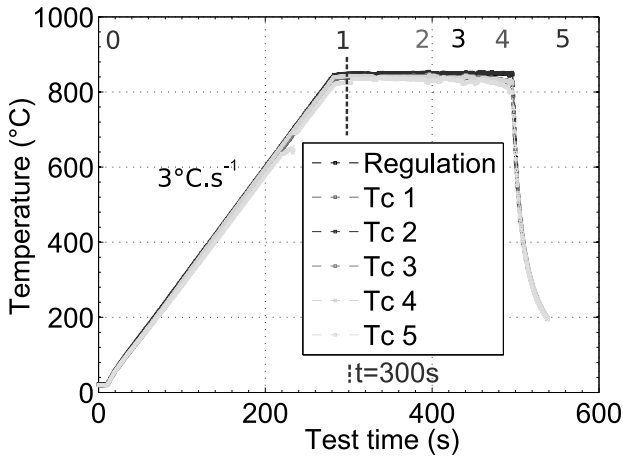


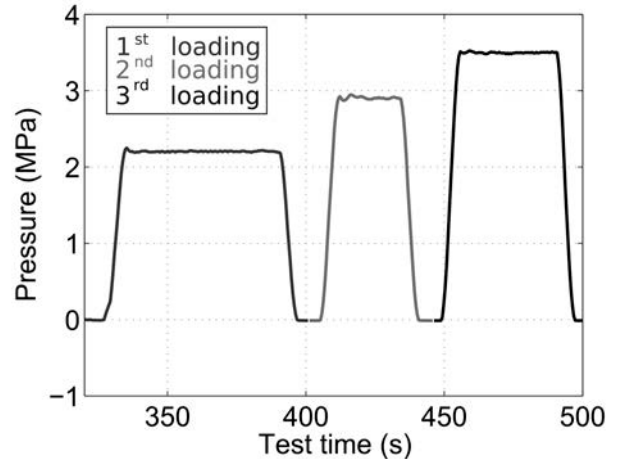
Figure 1: Schema and upper view of the experimental setup.

Argon flushing was controlled during the entire test. Tube heating rate was set to $\dot{T} = 3 \text{ }^{\circ}\text{C.s}^{-1}$ using an induction system controlled by a K-type thermocouple measurement regulation loop (Fig. 2a). The specimen is internally pressurized with argon. A proportional pressure regulator controlled the internal pressurization level. Three pressure levels were stepwise established (Fig. 2b). The pressure-induced bottom-end effect was mechanically compensated with the add of an axial compressive force F , calculated using the initial inner radius R_i and the internal pressure P_i (see equation (3)).

$$F = -P_i \cdot \pi \cdot R_i^2 \quad (3)$$



(a) Temperatures



(b) Internal pressure

Figure 2: Thermal and pressure histories during a test performed at 850 °C.

The setup components close to the tube are illustrated in Fig. 3. The design of the coil geometry, the induction heating device and the cooling of the grips led to a temperature gradient along with the specimen height. Four cameras were set up over the enclosure circumference as depicted in Fig. 4.

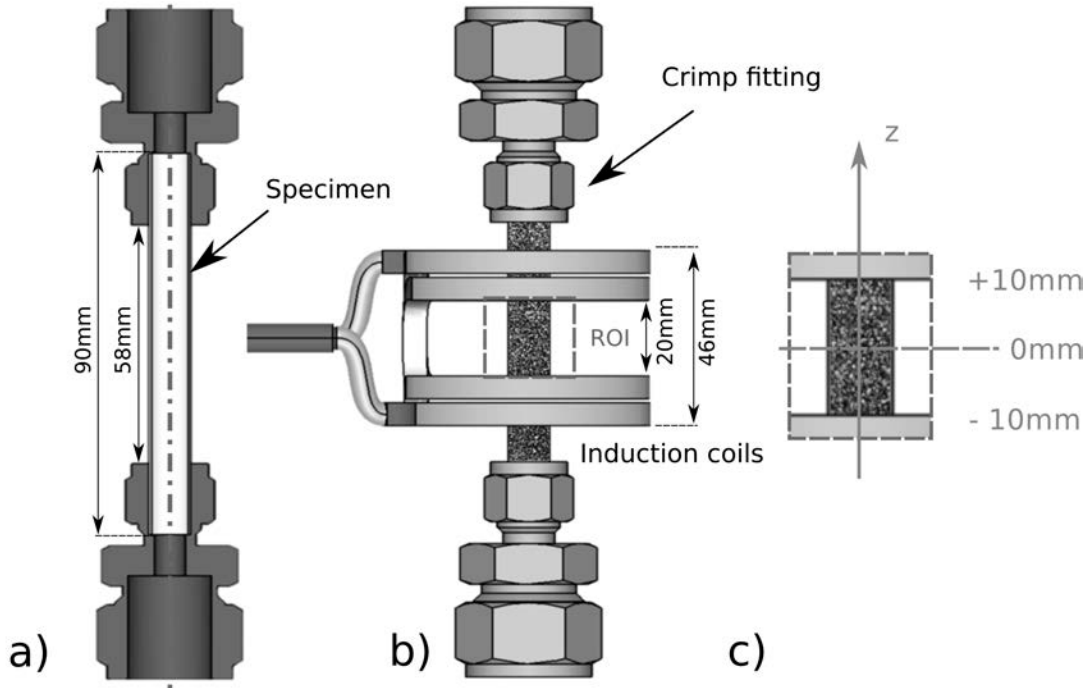


Figure 3: The geometries of the sample and the ROI are respectively detailed in a) and b). The test analysis datum is represented in c).

Cameras 1 & 2¹ were used for kinematics field measurement purpose. In order to get rid of incandescence, blue LED rings (CCS LDR2-70-BL2) were set up above and below the induction coils (see Fig. 1) as proposed by Pan *et al.* in [19, 20]. The LED rings were pulsing blue light. Band-pass filters² centered on 470 *nm* were fitted onto the cameras. Cameras 3 & 4³ were used to measure the thermal field by Near Infra-Red Thermography (NIRT). They were shooting pictures without any filtering when the blue lights were put off. The four cameras were fitted with 200 mm macro objectives (NIK AF MICRO-NIKKOR 200MM F/4 D IF-ED).

¹[VC-12MC-M65E0-FM] 12 MPx CMOS cameras.

²MIDOPT FIL BP470/62

³[Prosilica GE4900] 16 MPx CCD cameras.

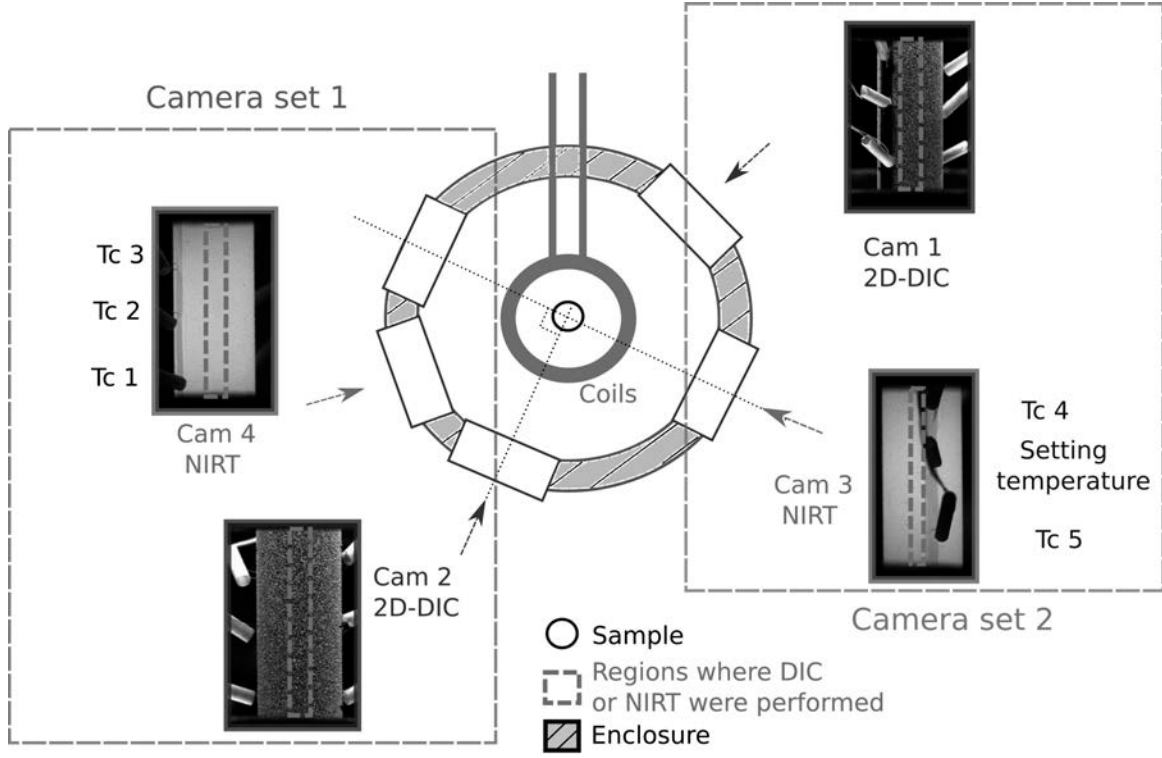


Figure 4: Distribution of the cameras over the enclosure.

The compressive force was measured by a 10 kN load cell, and the pressure by 5 MPa gauge sensors plugged into the upper and lower jaws. Several thermocouples were spot welded in the apparent ROI over the specimen's outer surface.

2.2. Experiment processing

The data measured by the camera set 1 (Fig. 4) are detailed below. The two key digital image analysis methods are reminded.

2.2.1. 2-Dimensional Digital Image Correlation

2D-DIC is performed using the software Ufreckles⁴ [21]. Axial and hoop displacement fields were calculated solving the conservation of the optical flow

⁴Developed by J. Réthoré at LaMCoS, INSA de Lyon

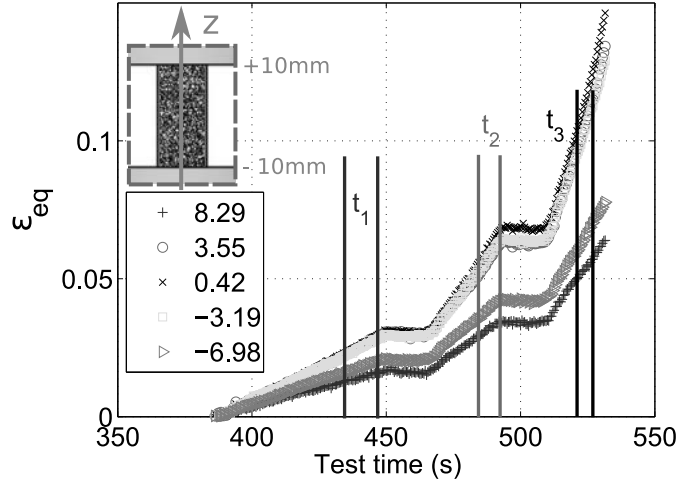
equation [22, 23]. A black undercoating (ULFALUX thermo-coating 1200 °C) was sprayed on the outer tube surface. A white speckle was then applied using BND painting. The speckle size ranged from 10 to 120 μm . Ufreckles uses a global FE-DIC approach. A typical Q4 element size was 30x30 px^2 ($1 \simeq 9 \mu\text{m}$). From the gradient tensors, logarithmic strains were computed. True equivalent creep strain was calculated over the sample surface assuming material incompressibility (equation (4)) during high temperature creep.

$$\begin{aligned} \epsilon_{zz}^{vp} + \epsilon_{\theta\theta}^{vp} + \epsilon_{rr}^{vp} &= 0 \\ \varepsilon_{eq}^{vp} &= \left[\frac{2}{3} (\varepsilon_{zz}^2 + \varepsilon_{\theta\theta}^2 + \varepsilon_{rr}^2) \right]^{\frac{1}{2}} \end{aligned} \quad (4)$$

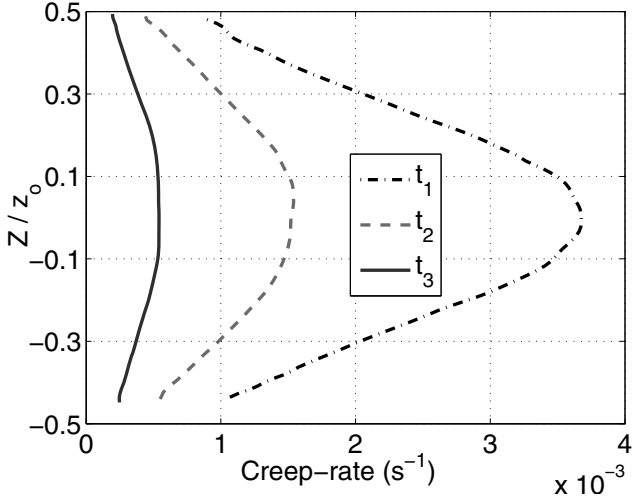
Typical processed areas are depicted in Fig. 4. They were small quadrant in front of the camera assumed as a plan during the processing. In the case of 2D-DIC, the displacements were extracted on the generator in front of the cameras using the FE interpolation. Systematic errors due to initial and ballooned geometries were estimated lower than 1% of the true equivalent strain up to 0.12 hencky strain [11]. Creep curves measured on the surface of a single specimen at five different axial positions are plotted in Fig. 5a. The steady-state creep-rate axial distributions at three different time steps are plotted in Fig. 5b versus normalized axial position. The different slopes correspond to the 3 internal pressure loadings (Fig. 2b).

2.2.2. Near Infra-Red Thermography

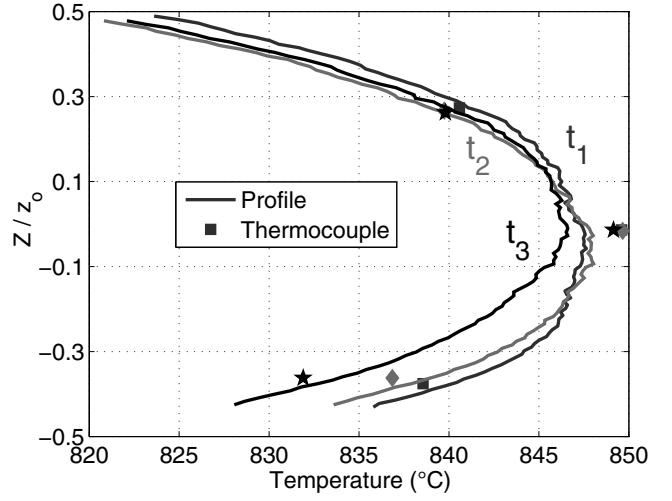
Near Infra-Red Thermography (NIRT) was used as a radiometer [24] in order to measure the thermal axial distribution. Light intensity I , captured by the silicon sensor of the cameras dedicated to NIRT, is directly linked to



(a) Creep curves



(b) Steady-state creep rates



(c) Temperature axial profiles.

Figure 5: The creep curves at five different axial locations (z is detailed in the legend) are plotted in (a) and creep-rate axial distributions calculated within the test periods t_1 , t_2 and t_3 are plotted in (b) versus the normalized axial position. Temperature axial profiles at the time periods associated to the creep-rate distribution calculation are plotted in (c).

the specimen surface radiation. The thermocouples (referenced in Fig. 4) Tc1, Tc2 and Tc3 allowed to determine the radiometric model detailed in equation (5), as detailed in [8]. Due to the speckle, an intensity threshold

was performed to process the pixels whose emissivity was the same.

$$T = \frac{K_1}{\ln\left(\frac{K_2}{I} + 1\right)}. \quad (5)$$

About ten profiles were extracted at different test times. The temperature distributions at t_1 , t_2 and t_3 are plotted versus the normalized axial position in Fig. 5c.

2.3. Test phenomenology

The specimen heating induces a thermal expansion of the tube. The axial temperature distribution leads to a stiffer cladding material close to the plugs. The internal pressure loading induces (from point 1 to 2 in Figs. 2a and 6) a hoop stress $\sigma_{\theta\theta}$ and a variation of axial stress σ_{zz} across the wall thickness due to bending. Note that the strains are measured over the outer surface of the sample where the stress state is not uniaxial.

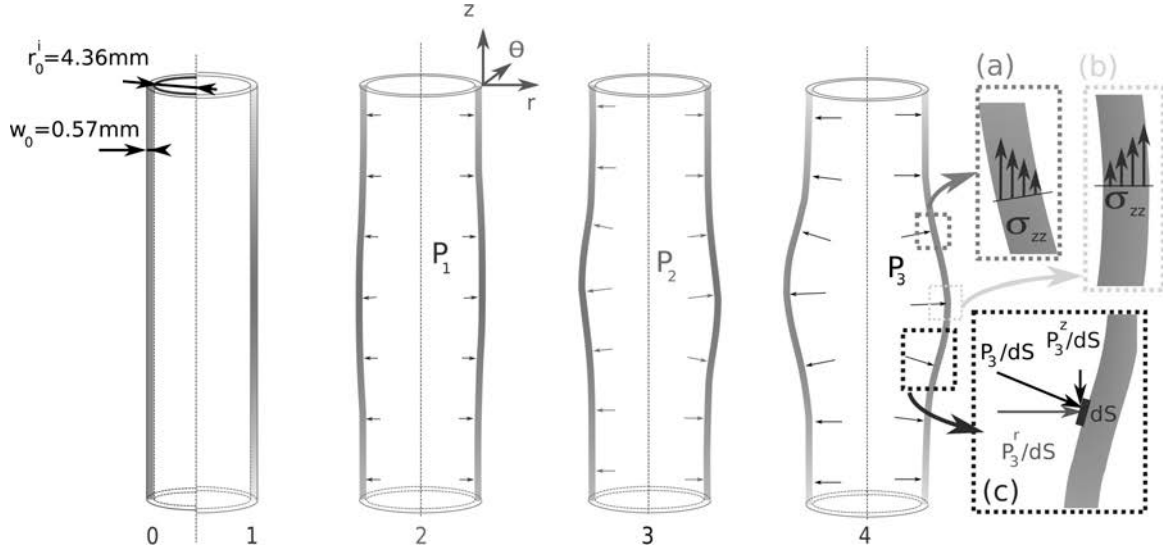


Figure 6: Evolution of the specimen during the deformation process (see Fig. 2a).

The combined effect of wall bending and temperature gradient induces

non uniform strain rate along the specimen height. The initial tubular geometry tends to balloon, leading to a complex heterogeneous stress state. Indeed, non-linear geometric effects respectively add compressive (a) and tensile (b) axial stresses on the cladding outer surface near the ROI borders and at its maximum formation location. In addition to this structural effect, the direction of pressure application follows the normal to the inner surface (c). The average axial stress across the wall thickness increases with tube ballooning so as the temperature axial heterogeneity. The hottest zones are located closest to the induction coils.

Finally, thermal and structural effects must be taken into account, relying on a FEMU process, in order to obtain an accurate evaluation of the secondary creep behavior of Zr-4 claddings.

2.4. FEMU algorithm

2.4.1. Test modeling

An overview of the different finite element model datings can be found in Réthoré [12]. The modeling of the boundary conditions affects the whole identification process. Experimental imperfections such as misalignment can be directly measured by DIC. It is thus often better to use the measured displacements as boundary conditions. This is of great importance when the borders are far (with respect to the characteristic dimensions) from the processed zone. Nevertheless, some kinematics assumptions have to be formulated in order to determine the boundary conditions through the thickness in a 3D or axi-symmetric calculation.

In the present study, since the bending of the wall induces non-uniform

displacements through the thickness, the whole specimen, up to the clamped ends, was modeled. Please recall that specific hydraulic clamping bushes guarantee a very small misalignment as demonstrated in [25] with the very reproducible measurements performed during the tension-torsion test.

Tests were modeled as axisymmetric using the commercial software Abaqus [26]. The part of the specimen located between plugs (58 mm long) was meshed using 6 regular CAX4I elements across its section (see Figure 7c). Element sizes were respectively 100 and 190 μm in the radial and axial directions.

Radial displacement of the two outer corner nodes and axial displacement of the outer middle node were blocked. The internal pressure was imposed using experimental data onto the inner tube surface.

The temperature axial profile was measured in the ROI using NIRT. Additional thermocouple measurements reported temperatures close to 500 °C at the plug locations. A sine sum model was fitted to these data. At least, three temperature profiles are calculated per internal pressure step. The sine sum models were implemented using the user subroutine UTEMP. A linear time interpolation was performed between these test times. An example of experimental temperature data and the fitted ones are plotted in Fig. 7a versus the axial position. The discrepancy is below 1 °C, as plotted in Fig. 7b.

Elastic behavior was modeled by a temperature-dependent Young's Modulus $E(T)$ [27] (equation (6) with T the temperature in Kelvin) and a Pois-

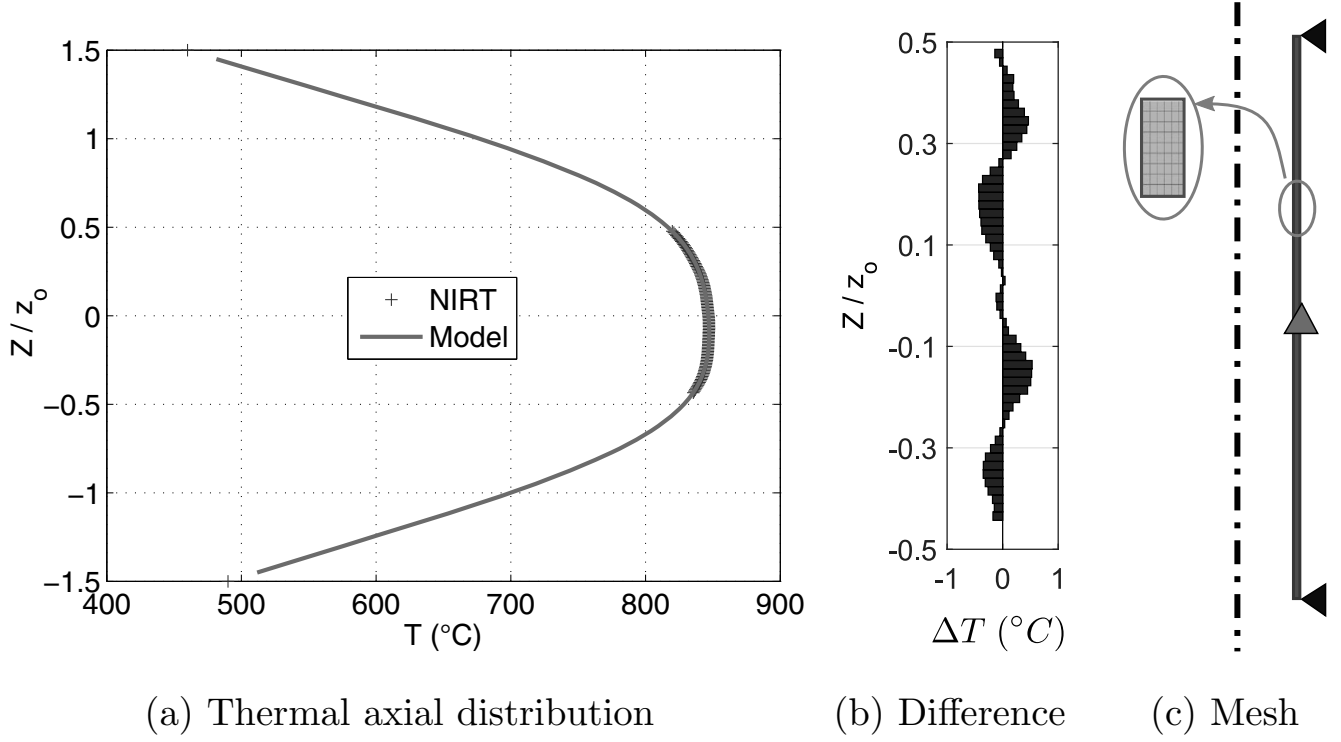


Figure 7: (a) Measured and fitted temperature axial distributions, and (b) their difference are plotted versus the normalized axial location. (c) The boundary conditions and the mesh of the modeling are represented.

son' ratio ν of 0.342. Thermal expansion was described by the coefficient α_{th} equal to $6 \cdot 10^{-6} \cdot \text{C}^{-1}$.

$$E(T) = 116.1 \cdot 10^3 - 59 \cdot T \quad [MPa] \quad (6)$$

The creep constitutive law of equation (1), still to be determined, was implemented using the CREEP subroutine of the ABAQUS program.

The model relied on two kinds of calculation steps, a static one corresponding to the specimen's heating and a time-dependent viscous one. The latter one was activated at the end of heating. The non-linear geometric effects were taken into account. Calculations were performed using Abaqus/Standard solver.

2.4.2. Algorithm

The main goal of this study is the determination of the constitutive creep law detailed in equation (1), and thus the quantification of A , n and Q in order to be able to predict the creep behavior of Zr-4 under LOCA conditions. FE calculations were performed and the error er (see Fig. 8) between the experimental measured data and the numerical one were computed. The cost function was chosen to only accounts for the 3 steady-state creep-rate axial distributions experimentally determined. The cost function was weighted using the experimental measurements in order to ensure the same influence of the three creep-rate profiles (that do not have the same magnitude). The problem was linearized using the steady-state creep-rate logarithms. The parameters optimization scheme is presented in Fig. 8. The method is based on a Gauss-Newton algorithm.

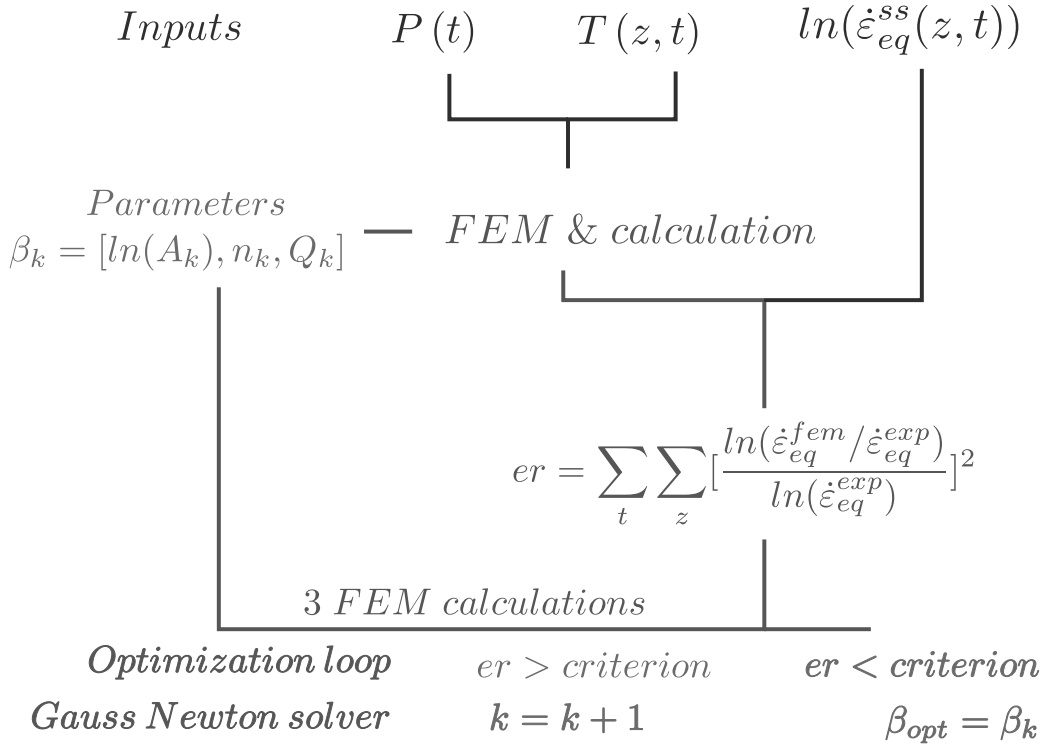


Figure 8: FEMU algorithm

A virtual testing, without noise, was performed for validation purposes. The error on the parameters was lower than 0.2%.

3. Results & discussion

The proposed methodology was applied to the test conditions described in Figs. 2 and 4. Experimental data resulting from the kinematics and thermal processing are plotted in Figs. 5b and 5c.

3.1. Application to a test

3.1.1. Constitutive behavior law parameters

Camera set 1 was first considered. The FEMU strategy led to the determination of the parameters $A = e^{32,8} \text{ MPa}^{-n} \cdot \text{s}^{-1}$, $n = 3.41$ and $Q = 466 \text{ kJ} \cdot \text{mol}^{-1}$. The creep-rates calculated at timestamps t_1 , t_2 and t_3 of the last FEMU were compared to the DIC measurements in Fig. 9.

The numerically calculated steady-state creep-rates are in good agreement with the 2D-DIC measurements. As reported by Hayes *et al.* in [5] Zr-4 is well described by Norton-type equations.

3.1.2. Equivalent strains and stresses

The constitutive behavior law was determined using the three steady-state creep-rates axial distributions.

The equivalent creep strains are in good agreement with experiments as illustrated in Fig. 10. The consistency between experiment and FE calculations demonstrates that the cladding behavior is governed by secondary

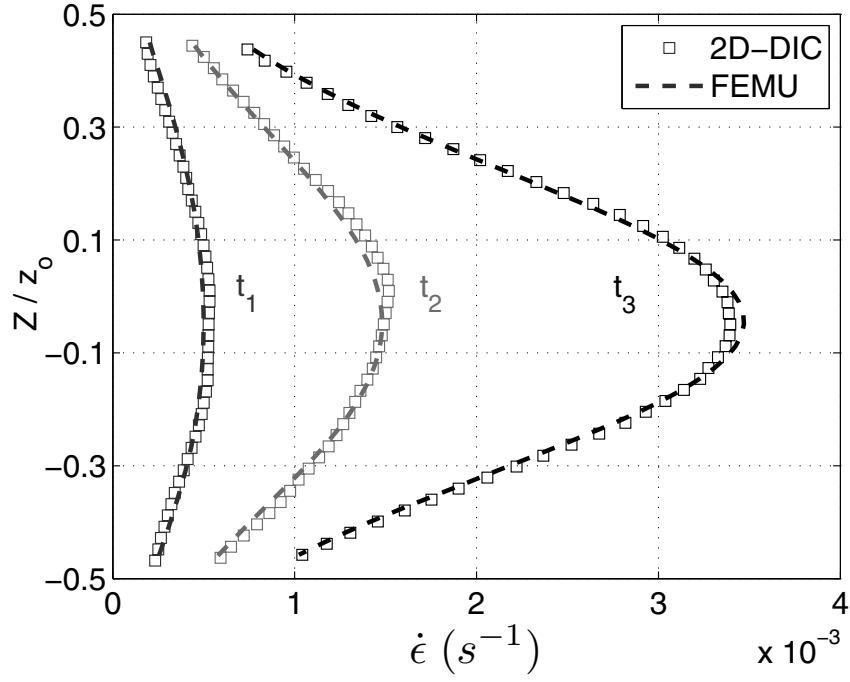


Figure 9: Comparison between the experimental and calculation creep-rate profiles based on camera set 1.

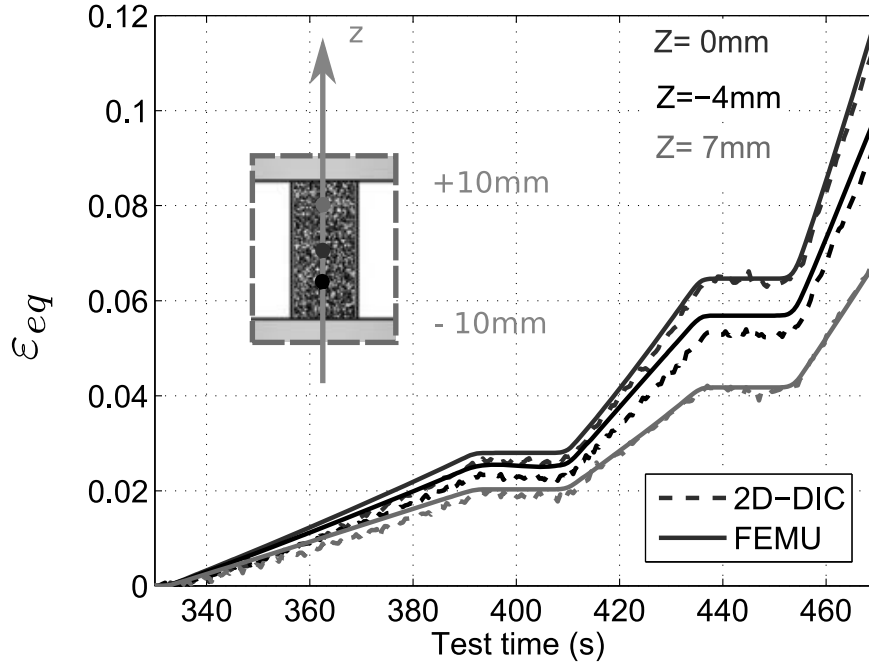


Figure 10: Equivalent creep strains over time.

creep only up to 12% strain. The values of the von Mises stress σ_{vM} , observed from FE calculation, at the outer tube surface are plotted in Fig. 11

versus normalized axial position at the three times of interest.

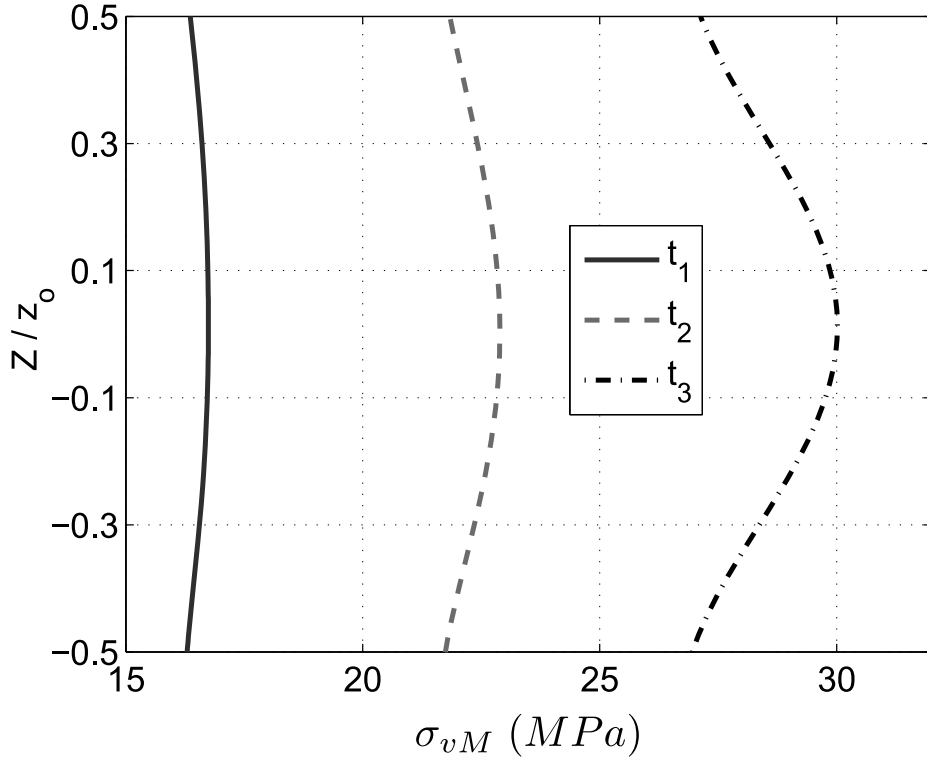


Figure 11: FE calculated equivalent stress distributions.

As the three steady-state creep-rate calculated and measured curves are consistent, the magnitudes of first and last equivalent stress distributions delineate the validity range in terms of stress of the determined constitutive behavior law. Hence, the set of parameters accounts for the creep behavior from 16 to 30 MPa and from 830 to 850 °C. Note that the duration of the specimen exposure to high temperature is representative of the LOCA conditions, since no thermal constant level was necessary before the application of the mechanical loading.

3.1.3. Axisymmetric assumption

The whole methodology relies on the axisymmetric assumption (modeling, both thermal and kinematics field measurements). We applied a thickness measurement in a r - θ plane at the end of a test as depicted in Fig. 12 in order to validate this assumption. Note that the hencky strain at the end of the third loading reached 0.3 and was thus far above the strain range used for the identification of the constitutive law (at most 0.12).

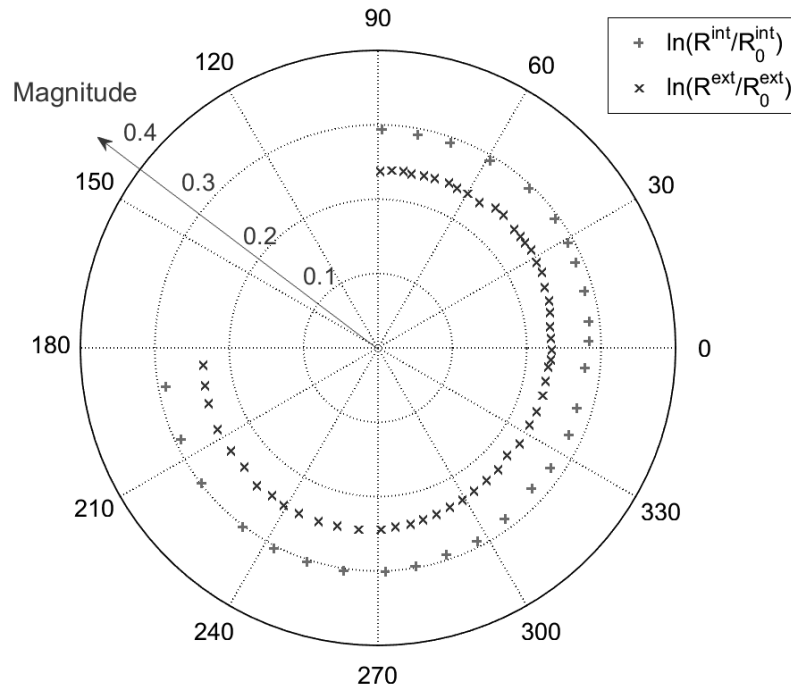


Figure 12: True hoop strains calculated from the measurements of internal and outer radius.

3.2. Analysis of nine tests

The proposed methodology was applied to several testings in order to determine the effect of both stress and temperatures levels on the creep

behavior of Zr-4 claddings.

3.2.1. Specimens

Nine experiments were performed under the thermal-mechanical conditions reported in Table 2.

Table 2: Settings of the experiments.

Specimen	Temperature (°C)	Internal pressures (MPa)			FEMU
	[min, max]	P_1	P_2	P_3	identification
AR-1	[831, 848]	1.04	1.65	2.24	2
AR-2	[831, 848]	2.17	2.89	3.51	1
AR-3	[810, 828]	2.75	3.33	3.86	2
AR-4	[781, 799]	1.48	2.66	⊘	1
AR-5	[778, 798]	2.75	3.33	3.86	2
AR-6	[780, 800]	4.03	4.52	5.04	2
AR-7	[747, 767]	3.05	3.70	4.89	2
AR-8	[755, 775]	2.60	3.35	4.25	2
AR-9	[785, 810]	3.90	4.30	⊘	1

3.2.2. Results

Table 3 summarizes the parameters derived from each test using one set of cameras. Note that the complex specimen preparation and setup potentially induced the loss of some of the thermocouples. The set of cameras was chosen in order to ensure the validity of the NIR thermography measurements and

Table 3: Parameters resulting from the FEMU method.

Specimen	Loadings	$\ln(A)$	n	Q	$< S_n >$
		A in $\text{MPa}^{-n} \cdot \text{s}^{-1}$		kJ/mol	
AR-1	1 & 2	46.6	1.08	543	0.079
-	2 & 3	47.5	2.15	576	0.051
AR-2	1 & 3	32.8	3.41	466	0.048
AR-3	1 & 2	14.2	2.77	283	0.062
-	2 & 3	17.8	2.89	317	0.062
AR-4	1 & 2	6.60	1.87	192	0.058
AR-5	1 & 2	9.48	1.16	198	0.024
-	2 & 3	-1.33	4.69	206	0.024
AR-6	1 & 2	-1.19	4.42	192	0.028
-	2 & 3	-5.18	5.08	178	0.040
AR-7	1 & 2	3.01	2.52	178	0.0341
-	2 & 3	-3.45	4.71	186	0.027
AR-8	1 & 2	0.47	1.27	123	0.032
-	2 & 3	-7.68	4.39	142	0.062
AR-9	1 & 2	6.16	3.98	223	0.056

to lower the angular distance between the selected cameras.

Note that the creep behavior can not be modeled systematically using the same constitutive law all over a single experiment gage surface. As illustrated by the parameters obtained for AR-5 specimen, the Norton exponent varied significantly even for a limited stress variation. For an accurate determination

of the parameters, the test data were split into two data sets. A first power-law was determined using the first two loadings, and then a second finite element model was updated using the last two loading steps. The change of geometry induced by the first internal pressure was taken into account to identify the constitutive parameters of the second step of the test.

The root mean square deviation $< S_n >$ detailed in equation (7) is also given in Table 3 in order to characterize the accuracy of the modeling. Note that there are about hundred measurement points, distributed along the generator, per internal pressure loading.

$$< S_n > = \sqrt{\frac{1}{n} \sum_{i=1}^n \left(\frac{\dot{\epsilon}_{eq}^{fem} - \dot{\epsilon}_{eq}^{exp}}{\dot{\epsilon}_{eq}^{exp}} \right)^2} \quad (7)$$

The steady-state creep-rates are plotted within their domain of validity in Fig. 13. One box corresponds to one identification step. The ranges in terms of stress and temperature were respectively determined using the FE calculation and the NIRT.

The observed consistency between the experiments is noteworthy and speaks not only to the repeatability of the performance, but also to the processing and the modeling of the experiments.

3.2.3. Comparison with literature data

In the literature [7, 6, 28], a great number of tests is required to identify creep parameters for given (or not) stress values. Furthermore, each test induces its own uncertainty.

The present experimental set up, combined with the measurement techniques, allowed us to identify creep parameters for stress and temperature

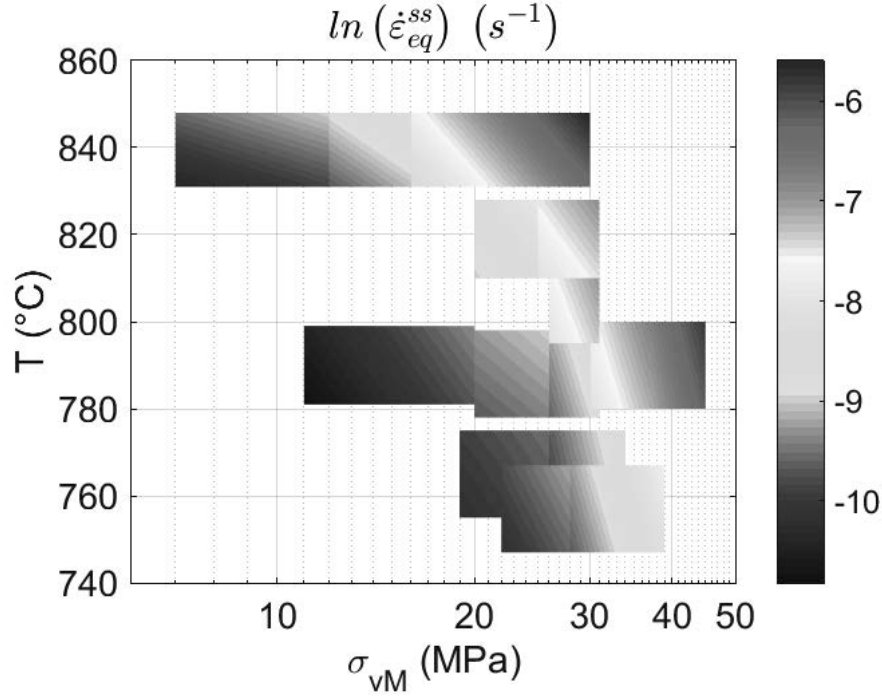


Figure 13: Steady-state creep-rate of all the full testing performed are plotted versus temperature and stress.

ranges, and to reduce the number of tests.

The influences of both stress σ_{vM} and the temperature T on the steady-state creep rate $\dot{\epsilon}_{eq}^{ss}$ were directly extracted from the present study. The Norton exponents, representing the effect of the stress on the creep-rate and associated to each test, are plotted in Fig. 14.

The temperature $T_{\alpha+\beta}$, at which the phase transformation $\alpha \rightarrow \alpha + \beta$ begins, is represented in Figs. 14 and 15 using a purple line.

The highest Norton exponent determined above $T_{\alpha+\beta}$ is 3.41. It was identified using the three internal pressure loadings of the AR-2 experiment so the stress's influence is constant from 16 to 30 MPa in this domain. Garde *et al.*[29] performed uniaxial tensile creep tests combined with metallography analysis. They evidenced a grain boundary sliding creep mechanism for

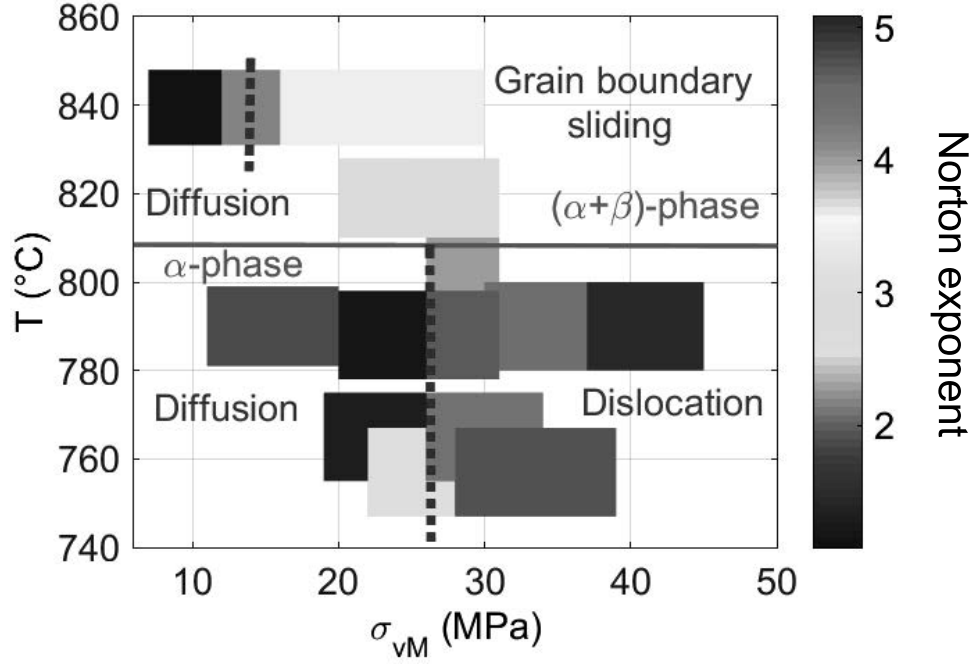


Figure 14: Norton exponents

temperature close to 850 °C. Their analysis provided a Norton exponent of 4.35 and an activation energy of 316 kJ/mol in a temperature range of 850 to 900 °C. More physically realistic creep diffusion modelings can be found in the literature [30, 31] explaining the superplastic deformation mechanisms experimentally observed by Garde *et al.*. A recent numerical work by Massih [32] couples such modeling with phase mixing in the two-phase domain in order to determine the creep behavior of zirconium alloys (Zr-1wt%Nb and Zircaloy-4). The Norton exponents accounting for the mixing phase model are determined as $n_\alpha = 3.45$ and $n_\beta = 3.35$. Our phenomenological approach gives n magnitudes similar to those obtained by the homogenization approach of Massih.

The transition from diffusion to assumed grain boundary sliding creep mechanism is observed for stresses from 12 to 16 MPa and temperatures from 830 to 850 °C.

Low stresses are characterized with a Norton exponent value close to unity in the α -phase domain. The literature associated to these temperature and stress ranges reports diffusion creep mechanisms in these conditions. Most of the constitutive laws for diffusion creep in the literature [33, 34] confirm a Norton exponent values near the unity. A clear change in Norton exponents is observed between low and high stresses in the α -phase domain at a critical stress of 26 MPa. The Norton exponent of 4.7 is in good agreement with dislocation climb creep mechanism reported in most experimental studies [7, 6] in the α -phase domain.

The activation energies, representing the effect of temperature on steady-state creep-rates, are plotted in Fig. 15.

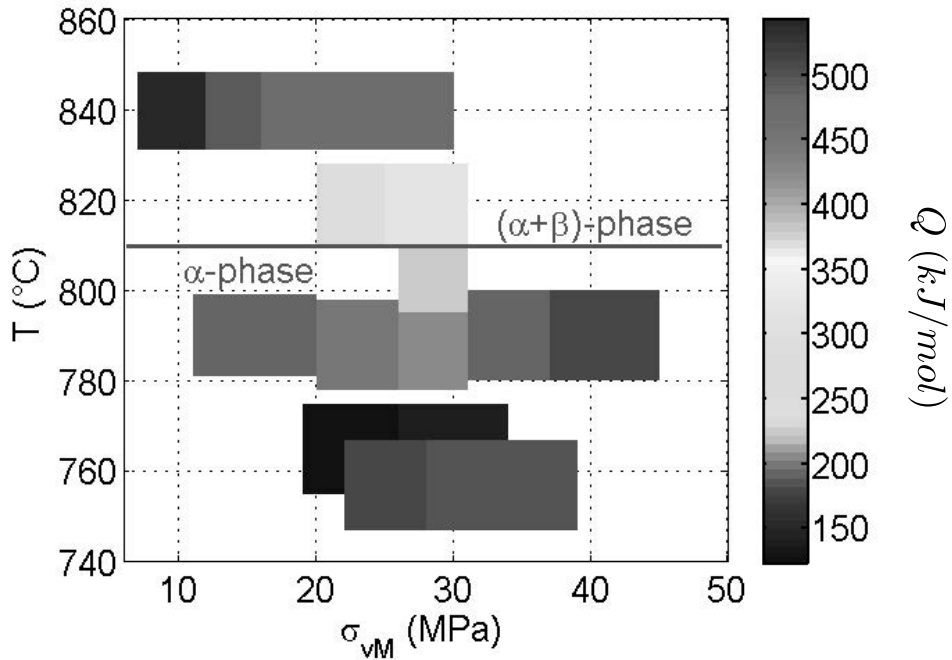


Figure 15: Activation energies.

We observe a clear transition in the activation energies at 810 °C. It corresponds to incipient phase transformation. The determined activation energies

are consistent in the α -phase domain.

The magnitude of Q increases in the $\alpha + \beta$ range. Note that Garde *et al.* reported activation energies decreasing with increasing stresses, and in a range of 270 to 352 kJ/mol. The same trend is observed here for temperature ranging from 830 to 850 °C (experiments AR-1 and 2).

3.3. Toward a correlation of the tests in the α -phase domain

The maps of the parameters n and Q , based on the identification of constitutive laws using the data of each individual test, illustrated the two creep mechanisms expected in the α -phase domain. For the purpose of severe accident detailed modeling, accounting for multi-physical phenomena, the data of several tests were combined to determine creep laws with validity domain covering a large range of temperature and stress. The data addressing to σ_{vM} (MPa) $\in [12, 26]$ obtained from tests on specimens AR-4,5,7 and 8 were used to assess the lower stress α -phase constitutive behavior law. The data addressing to σ_{vM} (MPa) $\in [26, 38]$, and $\dot{\varepsilon}_{eq}^{ss} \leq 3.10^{-4}$ derived from tests on specimens AR-5,7 and 8 were used to calculate the higher stress α -phase constitutive behavior law. The data of AR-6 and 9 specimens were finally used for modeling the highest creep-rates for temperatures from 780 to 809 °C. The parameters, their validity range, and the root mean square deviation are reported in Table 4.

The deviation $< S_n >$ of each of the identification remains lower than 20%. Finally, the activation energies determined at low and high stresses are consistent for low creep-rates. The activation energy determined for $\dot{\varepsilon}_{eq}^{ss} > 3.10^{-4} s^{-1}$ is higher than the energies calculated independently with each test data. Q and n magnitudes are consistent with those found in the

Table 4: Parameters identified in the α -phase domain.

T	σ_{vM}	$\dot{\epsilon}_{eq}^{ss}$	A	n	Q	$< S_n >$
°C	MPa	s^{-1}	$MPa^{-n}.s^{-1}$		kJ/mol	
748-798	12-26		$e^{2.46}$	1.66	150	0.095
748-798	26-38	$< 3.10^{-4}$	$e^{-6.95}$	4.95	163	0.094
780-809	30-47	$> 3.10^{-4}$	$e^{12.2}$	3.92	293	0.19

literature describing diffusion and dislocation creep mechanisms of Zr-4 in these temperature and stress ranges.

Conclusions and perspectives

A ballooning test was designed to investigate as-received SRA Zr-4 cladding secondary-creep behavior under simulated LOCA thermal-mechanical conditions. The specimens exposures duration to high temperature is representative of the LOCA conditions.

An axially heterogeneous thermal-mechanical loading was applied on a tubular specimen. Thermal and kinematic fields were measured along a generator. The large amount of data generated by the full field measurements was then used to determine the Zr-4 cladding steady-state creep behavior based on the von Mises criterion by FEMU:

- The setup enables to capture a 20 °C thermal heterogeneity. The thermal distribution perfectly correlates with the strain rate distribution. In addition three different internal pressures were applied during a test. A secondary creep constitutive power-law can be fully identified from a single test.

Hence, the methodology enables significant reduction of the number of tests required to determine the parameters.

- The methodology was applied to nine experiments performed for temperatures ranging from 747 to 848 °C, and internal pressures varying from 1 to 5 MPa. The steady-state creep-rate measurements of the nine tests were in a good agreement between each others. The constitutive creep-law parameters extracted from the FEMU were consistent with those in Ref. [7, 6]. Norton exponents usually associated to diffusion and dislocation creep mechanisms were determined in the α -phase domain for stresses respectively beyond and above a critical stress of 26 MPa. Constitutive laws addressing each of the mechanisms are proposed for the Zr-4 α -phase creep behavior modeling. The influence of the stress on the creep-rate is modified in the early stage of the two-phases domain. It could possibly correspond to the superplasticity exhibited for Zirconium and its alloys by some authors [29, 35] in the $(\alpha + \beta)$ -domain. This transition in n is supported by the increase of the activation energy observed around 810 °C. The magnitude of Q in the α -phase domain was fully consistent with literature data.

Future extensions of this research will focus on the influence of the working environment conditions (hydriding, oxydation) on the creep behavior of Zr-4 cladding under LOCA conditions. The actual running conditions have been selected in order to investigate the influence of combined microstructural, and thermal-mechanical conditions on the creep mechanisms. Results on pre-hydrided specimens will be compared with their as-received twin tests to highlight the influence of hydrogen presence. The proposed identifi-

cation method should also be appropriated to identify steady-state creep laws of hydrided specimens. The oxygen influence on the creep behavior of Zr-4 claddings will be further investigated using pre-hydrided and pre-oxidized specimens.

4. Acknowledgment

The study was performed in the framework of the PERFROI ANR project (n° ANR-11-RSNR-0017-01). The authors would like to acknowledge all the participants of the project: EDF, IRSN-SEREX, LEMTA, Ecole Centrale de Paris. The authors would also like to thank J. Réthoré for the open access to the Ufreckles software and A. Maynadier for helping with the NIR thermography method.

References

References

- [1] G. Repetto, C. Dominguez, B. Durville, S. Carnemolla, D. Campello, N. Tardif, M. Gradeck, The R&D perfroi project on thermal mechanical and thermal hydraulics behaviors of a fuel rod assembly during a loss of coolant accident, in: 16th International Topical Meeting on Nuclear Reactor Thermalhydraulics, 2015.
- [2] T. Forgeron, J. Brachet, F. Barcelo, A. Castaing, J. Hivroz, J. Mardon, C. Bernaudat, Experiment and modeling of advanced fuel rod cladding behavior under loca conditions: Alpha-beta phase transformation kinetics and edgar methodology, ASTM Special Technical Publication 1354 (2000) 256–278.

- [3] T. Torimaru, T. Yasuda, M. Nakatsuka, Changes in mechanical properties of irradiated zircaloy-2 fuel cladding due to short term annealing, *Journal of Nuclear Materials* 238 (2) (1996) 169–174.
- [4] M. E. Kassner, M. T. Pérez Prado, *Fundamental of creep in metals and alloys* (First edition), 2004.
- [5] T. A. Hayes, M. Kassner, Creep of zirconium and zirconium alloys, *Metallurgical and Materials Transactions A* 37A (8) (2006) 2389–2396.
- [6] H. E. Rosinger, P. C. Bera, W. R. Ciendening, The steady-state creep of Zircaloy-4 fuel cladding from 940 to 1873 K, Tech. Rep. AECL-6193, Atomic Energy of Canada Limited (1978).
- [7] D. Kaddour, S. Frechinet, A. Gourgues, J. Brachet, L. Portier, A. Pineau, Experimental determination of creep properties of zirconium alloys together with phase transformation, *Scripta Materialia* 51 (6) (2004) 515 – 519.
- [8] D. Campello, N. Tardif, M.-C. Baietto, M. Coret, J. Desquines, Secondary creep behavior of zr-4 claddings under loca conditions, in: *Top Fuel 2016*, 2016.
- [9] D. Campello, N. Tardif, M.-C. Baietto, M. Coret, J. Desquines, J. Réthoré, A. Maynadier, Thermo mechanical behavior of fresh zircaloy-4 under LOCA conditions, in: *PhotoMechanics*, 2015.
- [10] D. Campello, N. Tardif, M.-C. Baietto, M. Coret, J. Desquines, Thermo mechanical behavior of fresh zircaloy-4 under LOCA conditions, in: *13th*

International Conf. on Creep and Fracture of Engineering Materials and structures, 2015.

- [11] D. Campello, N. Tardif, A. Maynadier, M.-C. Baietto, M. Coret, J. Desquines, Design and validation of a multi-modal setup for the study of zirconium alloys fuel rods behavior under thermal mechanical conditions simulating a severe accident, In Press.
- [12] J. Réthoré, Muhibullah, T. Elguedj, M. Coret, P. Chaudet, A. Combescure, Robust identification of elasto-plastic constitutive law parameters from digital images using 3D kinematics, *International Journal of Solids and Structures* 50 (1) (2013) 73–85.
- [13] S. Avril, M. Bonnet, A.-S. Bretelle, M. Grediac, F. Hild, P. Ienny, F. Latourte, D. Lemosse, S. Pagano, E. Pagnacco, et al., Overview of identification methods of mechanical parameters based on full-field measurements, *Experimental Mechanics* 48 (4) (2008) 381–402.
- [14] K. T. Kavanagh, R. W. Clough, Finite element applications in the characterization of elastic solids, *International Journal of Solids and Structures* 7 (1) (1971) 11 – 23.
- [15] J.-C. Passieux, F. Bugarin, C. David, J.-N. Périé, L. Robert, Multiscale displacement field measurement using digital image correlation: Application to the identification of elastic properties, *Experimental Mechanics* 55 (1) (2015) 121–137.
- [16] P. Ienny, A.-S. Caro-Bretelle, E. Pagnacco, Identification from measurements of mechanical fields by finite element model updating strategies:

a review, *European Journal of Computational Mechanics/Revue Européenne de Mécanique Numérique* 18 (3-4) (2009) 353–376.

- [17] T. Link, D. Koss, A. Motta, Failure of zircaloy cladding under transverse plane-strain deformation, *Nuclear Engineering and Design* 186 (3) (1998) 379–394.
- [18] N. Tardif, M. Coret, A. Combescure, Experimental study of the fracture kinetics of a tubular 16MnNiMo5 steel specimen under biaxial loading at 900 and 1000°C. application to the rupture of a vessel bottom head during a core meltdown accident in a pressurized water reactor, *Nuclear Engineering and Design* 241 (3) (2011) 755 – 766.
- [19] B. Pan, D. Wu, Z. Wang, Y. Xia, High-temperature digital image correlation method for full-field deformation measurement at 1200 °C, *Measurement Science and Technology* 22 (1) (2011) 015701.
- [20] B. Pan, D. Wu, Y. Xia, An active imaging digital image correlation method for deformation measurement insensitive to ambient light, *Optics & Laser Technology* 44 (1) (2012) 204 – 209.
- [21] J. Réthoré, A fully integrated noise robust strategy for the identification of constitutive laws from digital images, *International Journal for Numerical Methods in Engineering* 84 (6) (2010) 631–660.
- [22] M. Sutton, W. Wolters, W. Peters, W. Ranson, S. McNeill, Determination of displacements using an improved digital correlation method, *Image and vision computing* 1 (3) (1983) 133–139.

- [23] T. C. Chu, W. F. Ranson, M. A. Sutton, Applications of digital-image-correlation techniques to experimental mechanics, *Experimental Mechanics* 25 (3) (1985) 232–244.
- [24] F. Meriaudeau, E. Renier, F. Truchetet, Temperature imaging and image processing in the steel industry, *Optical Engineering* 35 (12) (1996) 3470–3481.
- [25] N. Tardif, S. Kyriakides, Determination of anisotropy and material hardening for aluminum sheet metal, *International Journal of Solids and Structures* 49 (25) (2012) 3496–3506.
- [26] Hibbett, Karlsson, Sorensen, ABAQUS/standard: User’s Manual, Vol. 1, Hibbitt, Karlsson & Sorensen, 1998.
- [27] D. L. Hagrman, G. A. Reymann, Matpro-version 11: a handbook of materials properties for use in the analysis of light water reactor fuel rod behavior, Tech. rep., Idaho National Engineering Lab., Idaho Falls (USA) (1979).
- [28] C. Busby, K. Marsh, High temperature, time-dependent deformation in internally pressurized Zircaloy-4 tubing (LWBR Development Program), Tech. rep., Colorado Cooperative Wildlife Research Unit, Fort Collins (USA) (1974).
- [29] A. Garde, H. Chung, T. Kassner, Micrograin superplasticity in zircaloy at 850 c, *Acta Metallurgica* 26 (1) (1978) 153–166.
- [30] M. Ashby, R. Verrall, Diffusion-accommodated flow and superplasticity, *Acta Metallurgica* 21 (2) (1973) 149–163.

- [31] T. G. Langdon, The physics of superplastic deformation, *Materials Science and Engineering: A* 137 (1991) 1–11.
- [32] A. Massih, High-temperature creep and superplasticity in zirconium alloys, *Journal of Nuclear Science and Technology* 50 (1) (2013) 21–34.
- [33] T. A. Hayes, M. Kassner, R. S. Rosen, Steady-state creep of α -zirconium at temperatures up to 850 c, *Metallurgical and Materials Transactions A* 33 (2) (2002) 337–343.
- [34] J. Fiala, L. Kloc, J. Čadek, Creep in metals at intermediate temperatures and low stresses: a review, *Materials Science and Engineering: A* 137 (1991) 163–172.
- [35] P. Zwigl, D. C. Dunand, Transformation superplasticity of zirconium, *Metallurgical and Materials Transactions A* 29 (10) (1998) 2571–2582.